An Improved Synchronization Stability Method of Virtual Synchronous Generators Based on Frequency Feedforward on Reactive Power Control Loop

Xiaoling Xiong, *Member, IEEE*, Chao Wu, *Member, IEEE*, and Frede Blaabjerg, *Fellow, IEEE*

***Abstract*—The synchronization stability of the virtual synchronous generator (VSG) under grid fault is an important issue for maintaining stable operation in the power system. Existing work has pointed out a low-pass filter (LPF) with a sufficiently low cutoff frequency in the reactive power control loop (RPCL) can improve the transient stability. Yet, the underlying mechanism was unknown. Moreover, as a key index of VSG and precondition of synchronization stability, the frequency response is rarely studied. In this article, based on the linearized model for qualitative analysis, combined with the nonlinear model for quantitative analysis, the underlying mechanism of improving synchronization stability using an LPF in the RPCL is revealed. Furthermore, to avoid increasing the system order and solve the conflict between transient stability and frequency response, an improved synchronization stability method is proposed by feedforwarding the frequency difference between the VSG and grid to the RPCL. The frequency response is also acquired based on the combined linearized and nonlinear model, which shows that the frequency feedforward method can further enhance the frequency stability. How to design the coefficient of the frequency feedforward path with different inertia requirements is also presented. Finally, this method is verified by experimental results.**

***Index Terms*—Frequency stability, reactive power control loop, synchronization stability, virtual inertia, virtual synchronous generators (VSGs).**

I. Introduction

THE penetration of distributed energy resources connected to the electric power system (EPS) by voltage source converters (VSCs) is growing quickly [1]–[3]. As a result, the EPS becomes weaker as the ratio of synchronous generators (SGs) based generation decreases, indicating that the inertia of the power grid is reduced [4]. The decrease of inertia will jeopardize the frequency stability from two aspects: frequency deviation and the rate of change of frequency (RoCoF). First, lower inertia leads to a large frequency deviation during the disturbances, which is harmful to both SGs and loads. Besides, lower inertia will cause a high RoCoF, which might trip the generators and lead to cascading failure [5]–[7]. Thus, to avoid the adverse effects of the low-inertia characteristic, it is necessary to investigate optimized control strategies that can equip the VSCs with inertia.

The basic idea is to control the VSCs to mimic actual SGs by using the swing equation [8]–[17]. The inertia emulating methods can generally be divided into the following two categories. The first one is virtual synchronous generators (VSGs) [8]–[10], also called as virtual synchronous machines [11] or synchroconverter [12], which directly imitate the mechanical toque equation in the active power control loop (APCL). Another category is the generalized droop control, which implements the inertia by adding a low-pass filter (LPF) in the APCL [13], [14]. It has been proved that these two methods are equivalent to the inertia response [15], [16]. Furthermore, an adaptive inertia and damping method are proposed to further increase the frequency stability by employing different inertia during the frequency deviation and recovery process [17], [18].

Even though the VSGs can support the system inertia and improve frequency stability, it still suffers from other stability problems during different kinds of disturbances. Substantial research efforts have been devoted to the modeling and stability analysis under different grid conditions [19]–[21], [24]–[32]. However, most of them are concentrated on the small-signal stability analysis [19], [20], which are generally assessed by linearizing the system around a steady-state operating point. The linearized small-signal model is simple and can provide a clear physical insight into the stability issues. However, much dynamic information was missing during the linearizing procedure, especially for the nonlinear behaviors during large disturbances. Thus, the linearized model cannot be directly extended to analyze the synchronization stability of the VSGs during grid faults, such as grid voltage sag, as it is a large-signal nonlinear dynamic response [21]. Dynamic voltage restorers (DVRs) are an effective method to restore the load voltage during the grid voltage sag [22]. However, it can only support the voltage for a very short time due to the limited capacity of the energy storage system [23]. On the other hand, the additional space and

Manuscript received August 9, 2020; revised October 26, 2020 and December 8, 2020; accepted January 13, 2021. Date of publication January 19, 2021; date of current version May 5, 2021. This work was supported by the National Natural Science Foundation of China under Grant 51707065 and in part by the VELUX FOUNDATIONS under the VILLUM Investigator Grant REPEPS (Award: 00016591). Recommended for publication by Associate Editor C. N. M. Ho. *(Corresponding author: Chao Wu.)*

Xiaoling Xiong is with the State Key Laboratory of Alternate Electrical Power System with Renewable Energy Sources, North China Electric Power University, Beijing 102206, China (e-mail: xiongxl1102@ncepu.edu.cn).

Chao Wu and Frede Blaabjerg are with the Department of Energy Technology, Aalborg University, 9220 Aalborg, Denmark (e-mail: cwu@et.aau.dk; fbl@et.aau.dk).

Color versions of one or more of the figures in this article are available at https://doi.org/10.1109/TPEL.2021.3052350.

Digital Object Identifier 10.1109/TPEL.2021.3052350

equipment are very costly. Thus, the DVR is usually installed for sensitive load, not in all general applications. Therefore, the DVRs are not concerned in this article, which mainly focuses on improving the control method of VSG to ride through the grid fault, i.e., synchronization stability. Recently, the synchronization stability, which describes the ability of the VSG to maintain synchronization with the grid during grid fault, has received much research interest [24]–[32].

The transient dynamics of VSC with grid-forming control are analyzed in [24]. It has been found that there were no synchronization stability problems when the system with power synchronous control has equilibrium points after grid fault [24], [25], due to a first-order response of the APCL. However, due to the noninertia contribution, the RoCoF was very high, which means that the frequency changes sharply during the transient process. In [26] and [27], the transient stability of VSGs can be enhanced by reducing the active power reference and/or increasing the reactive power reference during grid voltage sag. These methods are easily implemented by just changing the power reference according to the faulty voltage. However, the disadvantage is that the steady-state performance is changed. According to the IEEE Standard 1547-2018 [28], it requires the VSGs to operate normally for 10 s without decreasing the active power when the grid voltage drops to 0.5–0.8 p.u. In order to avoid the change of power reference, there are also some works aimed at changing the control structure to enhance the transient stability. In [29] and [30], an adaptive inertia method is proposed to decrease the frequency deviation during the transient period, which is dependent on detecting the frequency and RoCoF. The adaptive inertia is changed based on the direction of frequency variation and RoCoF variation, which is complicated to implement, especially the differentiation element. In [31], an additional damping control method is proposed based on the Lyapunov's direct method, but the design method for the additional damping coefficient is absent. In [32], a mode-switching control method is presented for riding through even without an equilibrium point by changing VSG mode during the grid faults. However, the mode detection block is complicated based on combining the variation of frequency and active power, especially when the differentiation element is used. In [21], it has been found there is a conflict between the frequency response and the transient stability, indicating that large inertia may drive the VSG to crossover the unstable equilibrium point (UEP). However, the frequency response is a key index and requirement for the VSG. The precondition for synchronization stability enhancement is that frequency stability should be first guaranteed.

In order to keep a high inertia contribution, using an LPF with a sufficiently low cutoff frequency in the RPCL can enhance transient stability. However, the underlying mechanism is not analyzed in details in [21]. Despite this, this method will decrease the dynamic performance of RPCL and increase the system order.

This article is going to solve the abovementioned problems. In addition, it aims to investigate an improved control method to enhance transient stability and not to deteriorate frequency stability simultaneously. Therefore, the contributions of this article can be summarized as follows.

1) An analytical method of combining linearized and nonlinear model is employed to study synchronization stability and frequency stability. The linearized model is used for qualitative analysis to provide physical meaning, while the nonlinear model is adopted for quantitative analysis and stability assessment.
2) The underlying mechanism of improving synchronization stability using an LPF in the RPCL is revealed. The added LPF introduces a dominant closed-loop pole to damp the power angle oscillation during the transient process. However, the system order is increased, and the dominant pole might jeopardize the VSG's small-signal stability.
3) In order to avoid the LPF with very low bandwidth in the RPCL, a frequency feedforward path is added in the RPCL to improve the synchronization stability without increasing the system order and not affecting the small-signal stability.
4) The synchronization stability and frequency response are studied based on the combined model, demonstrating that the frequency feedforward method can improve not only the synchronization stability but also the frequency stability during grid faults.

The rest of this article is organized as follows. The configuration and the basic mathematical model of the VSG are presented in Section II. In Section III, using the linearized method for qualitative analysis and the state-space trajectories of the nonlinear system for the quantitative analysis, the effect of LPF in RPCL on the synchronization stability is studied and revealed. Section IV proposes an improved method by adding a frequency feedforward path to the RPCL to enhance synchronization stability. Meanwhile, the frequency response is also derived based on the combined model. Detailed parameter design guidelines of the coefficient parameters for the additional path are also presented. The theoretical analysis is verified in Section V by experimental results. Finally, the conclusion is drawn in Section VI.

II. Configuration and Mathematical Model

The configuration of a three-phase grid-connected VSG is shown in Fig. 1. The grid is modeled as an infinite voltage in series with an impedance, which includes an inductance L_g and a resistance R_g. Here, $\mathbf{V_g} = \mathbf{V_g}\mathbf{e}^{\mathbf{j}\omega_\mathbf{g}\mathbf{t}}$ and $\mathbf{V_{pcc}} = V_{pcc}e^{j\theta_{pcc}}$ represent the space vectors of the grid voltage and the PCC voltage, respectively. Usually, ω_g is equal to the synchronous angular frequency ω_0 in a strong grid, but it varies when connected to a weak grid. Inductor L_f represents the output filter of the VSG, and $\mathbf{I}_g$ is the current vector of the injected current to the grid. P and Q represent the active and reactive power transferred from PCC to the grid, respectively. In practice, to make an inertia contribution, a large capacitor is added on the dc side, which is controlled by the front-end converter, or the energy storage is generally employed where the dc-link voltage is regulated by an energy storage converter [33], [34]. Hence, the dc voltage can

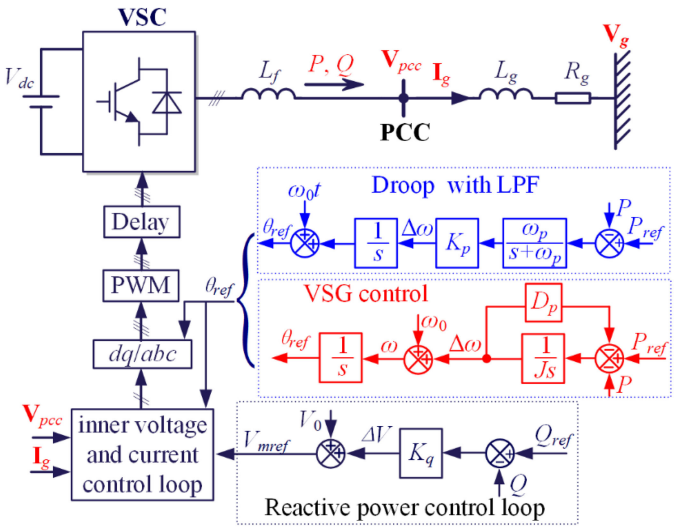

Fig. 1. Configuration of a three-phase grid-connected VSG.

be assumed to be constant when analyzing the synchronization issues between the VSG and the power grid [16], [21], [24]–[27].

As shown in Fig. 1, P_{ref} and Q_{ref} are active and reactive power references, respectively. The outer power control loops generate the PCC voltage vector reference, i.e., $\mathbf{V_{ref}} = \mathbf{V_{mref}} e^{j\theta_{ref}}$, where θ_{ref} and V_{mref} are the phase and the voltage amplitude reference, respectively. An inner voltage and current control loop are adopted to regulate $\boldsymbol{V}_{pcc}$ to track $\boldsymbol{V}_{ref}$ and limit the overcurrent. In practice, the responses of the outer power control loops are very slow, which determines the synchronization stability. Meanwhile, the inner loop bandwidth is much higher, and the delay term mainly affects the performance of high frequency [35], [36]. Therefore, the inner control loop and delay can be regarded as one with an ideal PCC voltage reference tracking when analyzing the synchronization stability [21], [24]–[27]. Thus, $V_{pcc} = V_{mref}$, $\theta_{pcc} = \theta_{ref}$ can be obtained.

The droop control with an LPF can be used to emulate the VSG control, where K_p is the proportional gain, ω_p is the cutoff angular frequency of LPF, which is added to provide virtual inertia. The commonly used VSG control scheme is also shown in Fig. 1, where J and D_p are the virtual inertia and the gain of frequency governor, respectively. The two control methods are equivalent when

$$J = \frac{1}{(K_p\omega_p)}, \qquad D_p = \frac{1}{K_p} \tag{1}$$

The droop control with an LPF is adopted in this article to compare with the results in [21] directly. The APCL is to emulate the swing equation of an SG, given as

$$d\omega/dt = K_p\omega_p\left(P_{ref} - P\right) - \omega_p\left(\omega - \omega_0\right). \tag{2}$$

The Q–V droop control is employed to adjust V_{mref}, the transfer function of which is given by

$$V_{mref} = V_0 + K_q \cdot (Q_{ref} - Q) \tag{3}$$

where K_q is the proportional gain.

Defining δ as the power angle, which is the phase difference between $\boldsymbol{V}_{pcc}$ and $\boldsymbol{V}_g$, i.e., $\delta = \theta_{pcc} - \theta_g = \theta_{ref} - \omega_g t$. Thus, P and Q can be derived as

$$P = \frac{3}{2}\frac{\left(V_{pcc}^2 - V_{pcc}V_g\cos\delta\right)R_g + X_g V_{pcc}V_g\sin\delta}{R_g^2 + X_g^2} \tag{4}$$

$$Q = \frac{3}{2}\frac{\left(V_{pcc}^2 - V_{pcc}V_g\cos\delta\right)X_g - R_g V_{pcc}V_g\sin\delta}{R_g^2 + X_g^2} \tag{5}$$

It can be found P and Q are coupled with each other, which gives the inspiration to provide damping from the RPCL. It will be discussed in details in Section IV.

III. Synchronization Stability Analysis

A. Types of the Synchronization Problems

Substituting (5)–(3) and considering $V_{pcc} = V_{mref}$, V_{pcc} can be solved. V_{pcc} is then substituted into (4), P–δ relationship can thus be obtained in (6) shown at the bottom of this page, where

$$k_1 = \frac{X_g}{\left(R_g^2 + X_g^2\right)} \quad k_2 = \frac{R_g}{\left(R_g^2 + X_g^2\right)}. \tag{7}$$

Accordingly, the $P-\delta$ curves, with different grid voltage sags and different R_g, are plotted in Fig. 2. Assuming $\omega_g = \omega_0$ holds after a disturbance for simplifying the illustration. In Fig. 2(a), as shown by the solid line, the VSG initially operates at point a. After the disturbance occurs, there are two types of transient problems, i.e., the equilibrium point exists or not after the grid fault. According to IEEE Standards 1547-2018 [28], it can be known that the VSG should continue to supply power at least for 10 s when the grid voltage drops to 0.5–0.8 p.u. Ten seconds is undoubtedly larger than the critical clearing time of VSG, which indicates that the VSG should keep working normally during the fault for a long time. Therefore, this article aims to optimize the control algorithm to ride through the grid fault when the equilibrium point exists, as shown with the dashed red line. The points b and b_1 are the stable equilibrium point (SEP), and the UEP after disturbance, respectively. The corresponding power angles are denoted as δ_e and δ_{ce}. During the transient period, if the system goes across b_1, δ will exceed δ_{ce} and then go to infinite, causing the loss of synchronization (LOS). Thus, δ_{ce} is called the critical power angle. In contrast, if the power angle

$$P = \frac{3}{2}\frac{V_g\sin\delta}{X_g}\frac{1.5k_1K_qV_gcos\delta + 1.5k_2K_qV_g\sin\delta - 1 + \sqrt{\left(1.5k_1K_qV_gcos\delta + 1.5k_2K_qV_g\sin\delta - 1\right)^2 + 6k_1K_q(V_0 + K_qQ_{ref})}}{3K_qk_1} \tag{6}$$

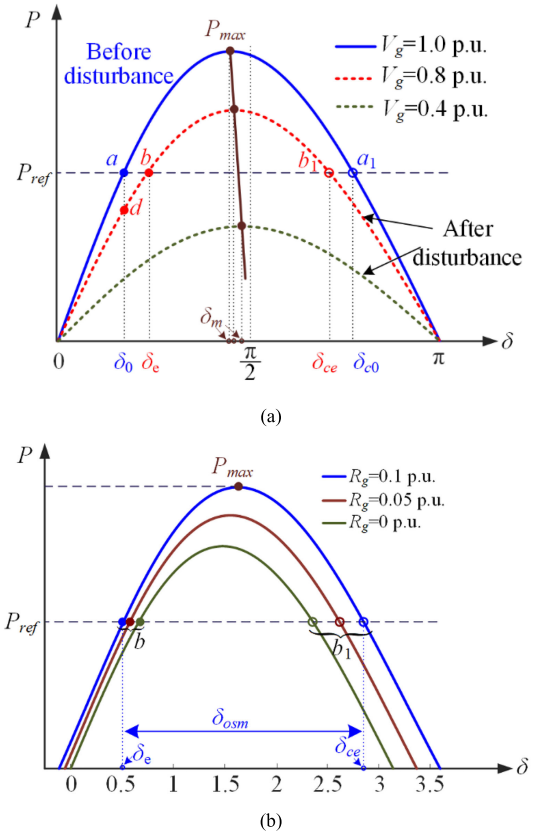

Fig. 2. *P*–δ curves with (a) different grid voltage sags and (b) different grid resistances R_g.

was controlled smaller than δ_{ce} during the transient period, the system finally can operate stably at *b*.

The other type of no equilibrium point after the fault, shown as the dashed green line, is not of concern here since it cannot continue supplying power normally.

From Fig. 2(b), it can be seen that the power transfer capability of the VSG varies with different R_g. The maximum power P_{max} that can be transmitted becomes higher with a larger R_g. Meanwhile, the allowed variation range of the power angle δ, i.e., δ_{osm}, is much wider with a larger R_g, which can benefit the synchronization stability during grid fault. Thus, the worst condition is $R_g = 0$, which is focused on in this article.

B. Effects of the LPF in the Reactive Power Control Loop

As shown in Fig. 2, after the grid fault, the SEP *b* is small-signal stable; thus, all the trajectories of the state variables in the neighborhood are attracted to *b*. However, how large the neighborhood is unknown. The severe grid faults might be out of the neighborhood, resulting in the small-signal stability analysis method is not accurate enough to investigate transient stability. However, the linearized model can provide clear physical insight and intuitive explanation of stability issues, which is, thus, considered to be used for a better understanding. Before that, the connections between the linearized model and the nonlinear model should be established. Suppose the VSG is large-signal

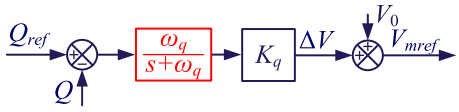

Fig. 3. LPF is added in RPCL in [21] to enhance the transient stability.

stable. In that case, it will finally be attracted to the neighborhood of *b* (see Fig. 2), so the trajectory for the original nonlinear system has the same response trend as the linearized system. For example, a larger damping ratio leads to a smaller overshoot for a linear second-order system, which is also applicable to the nonlinear system. Therefore, the linearized system can be used for qualitative analysis during the grid faults, such as analyzing the overshoot and the damping ratio for the power angle response.

In [21], it has been revealed that adding an LPF in the RPCL, as shown in Fig. 3, with a very low cutoff frequency ω_q can enhance transient stability. However, the underlying mechanism is not addressed, and this article will give a thorough qualitative analysis based on the linearized method and quantitative analysis with the nonlinear system.

According to the previous description, the dynamics of the system is a third-order nonlinear system, which can be represented in the standard form as

$$\begin{bmatrix} \dot{x}_1 \\ \dot{x}_2 \\ \dot{x}_3 \end{bmatrix} = \begin{bmatrix} x_2+\omega_0-\omega_g \\ -\omega_p x_2 - \frac{3\omega_p K_p V_g x_3}{2X_g}\sin x_1 + \omega_p K_p P_{ref} \\ \omega_q (V_0 - x_3) \\ \quad +\omega_q K_q \left(Q_{ref} - \frac{3}{2}\frac{{x_3}^2 - V_g x_3 \cos x_1}{X_g} \right) \end{bmatrix} \tag{8}$$

where dot $(\cdot)$ denotes time derivative, $\boldsymbol{x} = [x_1, x_2, x_3]^T = [\delta, \Delta\omega, V_{pcc}]^T$ is the state variable vector, and superscript *T* represents the transposition of a matrix or vector.

By setting all the differential items in (8) to zero, the two equilibrium points $\boldsymbol{x_e} = [\delta_e, \Delta\omega_e\ V_{pcce}]^T$ and $\boldsymbol{x_{ce}} = [\delta_{ce}, \Delta\omega_{ce}\ V_{pccce}]^T$ can be obtained. This implies $\Delta\omega_e = \Delta\omega_{ce} = \omega_g - \omega_0$, δ_e (δ_{ce}) and V_{pcce} (V_{pccce}) should satisfy

$$\begin{cases} \dfrac{3}{2}\cdot\dfrac{V_g V_{pcc}\sin\delta}{X_g} = P_{ref} - \dfrac{\omega_g-\omega_0}{K_p} \\ V_{pcc} = V_0 + K_q\left(Q_{ref} - \dfrac{3}{2}\cdot\dfrac{V_{pcc}^2 - V_{pcc}V_g\cos\delta}{X_g}\right). \end{cases} \tag{9}$$

By solving (9), $V_{pcce} = V_{pccce}$, and two angle values in [0, 2π] for δ can be obtained. Among them, the smaller one is δ_e, and the other larger one is δ_{ce}. The equilibrium points are the same as the second-order system without LPFs.

To linearize the third-order system around the equilibrium point, the Jacobian $\boldsymbol{J}(\boldsymbol{x}_e)$ is calculated as

$$\boldsymbol{J}(\mathbf{x_e}) = \begin{bmatrix} 0 & 1 & 0 \\ -\dfrac{3\omega_p K_p V_g V_{pcce}\cos\delta_e}{2X_g} & -\omega_p & -\dfrac{3\omega_p K_p V_g \sin\delta_e}{2X_g} \\ -\dfrac{3\omega_q K_q V_g V_{pcce}\sin\delta_e}{2X_g} & 0 & J_{33} \end{bmatrix} \tag{10}$$

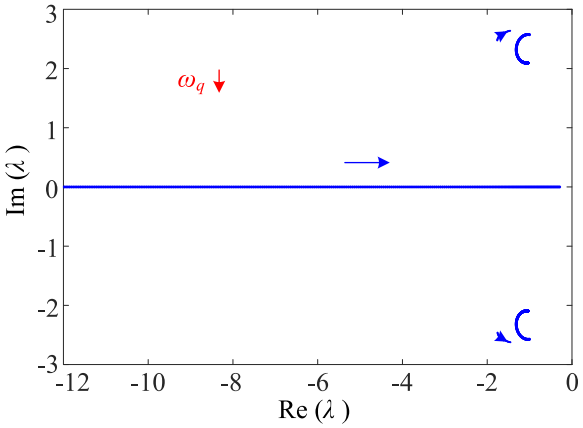

Fig. 4. Loci of eigenvalues with ω_q are decreasing from 4π to 0.1π rad/s ($\omega_p = 0.6\pi$ rad/s and $V_g = 0.6$ p.u.).

where J_{33} is

$$J_{33}=\frac{-2X_g\omega_q - 3\omega_q K_q(2V_{pcce} - V_g\cos\delta_e)}{2X_g}. \tag{11}$$

Suppose the eigenvalues (also called the closed-loop poles) of $\boldsymbol{J}(\boldsymbol{x}_e)$ include a real and a pair of conjugate eigenvalues. In that case, the system is decomposed into a first- and second-order dynamics. Thus, the response consists of an exponential curve and a damped sinusoidal curve. For a stable third-order system, if one pole is much closer to the imaginary axis than the other poles, it is called the dominant pole since this pole will determine the transient response and decay slowest.

To obtain the closed-loop poles, we can solve the characteristic equation for $\boldsymbol{J}(\boldsymbol{x}_e)$, i.e., $\det[\lambda\boldsymbol{I} - \boldsymbol{J}(\boldsymbol{x}_e)] = 0$. Suppose λ_1 is the pole for the first-order system, and $\lambda_{2,3}$ are the second-order system's conjugate eigenvalues. β denotes the ratio of the real parts of the poles, defined as $\beta = \text{Real}(\lambda_{2,3})/\lambda_1$. A large β helps us to dampen the oscillation of the second-order system, thus reducing the overshoot of the power angle and improving the synchronization stability. In contrast, if β is too small, i.e., $\beta < 0.1$, the system is dominated by the second-order system, and the impact of λ_1 is so little that it can be neglected. If β is sufficiently large, λ_1 is the dominant pole, and the approximated system can be a first-order one. To conclude, introducing an LPF in the RPCL means introducing a closed-loop pole λ_1, which can enhance the transient stability if it is close enough to the imaginary axis.

Numerical calculations are performed with ω_q decreasing from 4π rad/s to 0.1π rad/s when $V_g = 0.6$ p.u. and $\omega_p = 0.6\pi$ rad/s, the other parameters in Table III in Section V are adopted. The corresponding loci for eigenvalues are plotted in Fig. 4, and the typical scenario for the variation of the eigenvalues is shown in Table I. It can be found that ω_q mainly determines the real pole and has a little effect on the pair of conjugate eigenvalues. Smaller ω_q, such as $\omega_q < 0.4\pi$ rad/s, can make λ_1 closer to the imaginary axis, indicating the first-order system dominates the system response in this case. Thus, smaller ω_q induces a larger β to damp the power angle overshoot, which can enhance the synchronization stability. As ω_q increases, the impact of λ_1 is reduced, and if $\omega_q \geq 2.6\pi$ rad/s, the impact can be ignored.

TABLE I
EIGENVALUES FOR INCREASING ω_q OF THE SYSTEM IN TABLE III

ω_q (rad/s)	Eigenvalues (λ_1, $\lambda_{2,3}$)	β
0.1π	-0.2910, $-1.0033 \pm j2.5724$	3.4478
0.2π	-0.5716, $-1.0694 \pm j2.5728$	1.8709
0.4π	-1.1354, $-1.2001 \pm j2.5250$	1.0570
0.44π	-1.2541, $-1.2234 \pm j2.5075$	1.0251
0.6π	-1.7729, $-1.2941 \pm j2.4153$	0.9755
π	-3.4718, $-1.2700 \pm j2.1857$	0.3658
2π	-7.9490, $-1.0948 \pm j2.0937$	0.1377
2.6π	-10.5049, $-1.0549 \pm j2.0924$	0.1004
20π	-82.5118, $-0.9552 \pm j2.1131$	0.0116

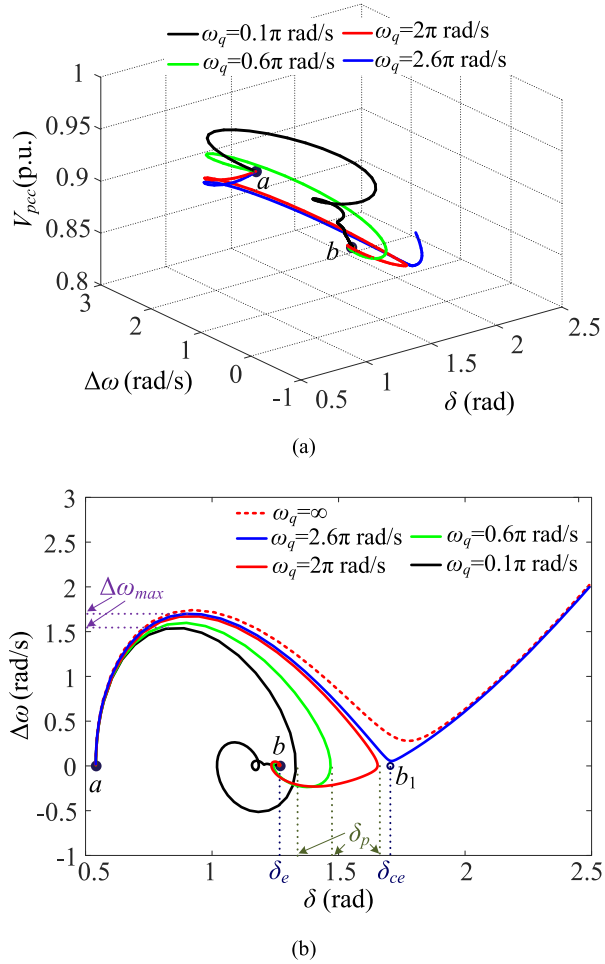

Fig. 5. State-space trajectories of the nonlinear system in (8) with different ω_q. (a) Corresponding trajectories of the third-order system. (b) Projection of $\Delta\omega$-δ plane to provide visual support. ($\omega_p = 0.6\pi$ rad/s and $V_g = 1 \rightarrow 0.6$ p.u.).

Although these conclusions are summarized with the linearized system, it can be applied to qualitatively evaluate the influences of the LPF in the RPCL for the nonlinear system.

To further investigate the impacts of ω_q and to obtain more accurate results, the state-space trajectories based on the original nonlinear system in (8) can be plotted, as shown in Fig. 5(a). To provide a more clear visual support, one of the projections, i.e., $\Delta\omega$-δ curves, is replotted in Fig. 5(b), where the second-order

system's unstable curve without LPF in the RPCL is also given to make a comparison. The power angle overshoot, denoted as δ_p, is the maximum difference between the transient power angle and δ_e, as shown in Fig. 5(b).

From Fig. 5, it can be found that a smaller ω_q damps more power angle overshoot, leading to better transient stability. If ω_q is small enough, as $\omega_q = 0.1\pi$ rad/s, indicating λ_1 is the dominant closed-loop pole, so the dynamic response behaves similarly as a first-order system in the neighborhood. If ω_q increases over 2.6π rad/s, the impacts of ω_q can be almost ignored. The responses of the nonlinear system agree with the qualitative analysis in Fig. 4 based on the linearized system.

However, only reducing ω_q, is not able to achieve an over-damped system during the grid fault. Take $\omega_q = 0.1\pi$ rad/s in Fig. 5 as an example. Although ω_q is small enough, the overshoot of δ still exists when the grid voltage drops from 1 to 0.6 p.u. Meanwhile, a sufficiently small ω_q can enhance transient stability but reducing the small-signal stability margin, as λ_1 is too close to the imaginary axis.

Moreover, the LPF is usually employed for Q–V droop control to filter the high-frequency harmonics and noises [8], [13], [14], ω_q is at least higher than 10 Hz, i.e., 1000 rad/s is used in [8]. Thus, the effect of this kind of LPF can be generally ignored when studying the synchronization stability issues due to the decoupled timescales. Here, the LPF is employed to simultaneously enhance the synchronization stability, ω_q needs to be set very low, such as lower than 2π rad/s. In this case, the effects of LPF cannot be ignored when analyzing the synchronization stability. Thus, the dynamics of the system are increased to third order. Unlike in the linearized second-order system, the underlying mechanism and the performance can be analyzed using an explicit mathematical approach rather than a numerical analysis. Therefore, in order to avoid these negative effects of too small ω_q, adding frequency feedforward to the RPCL is proposed to enhance the synchronization stability in Section IV.

IV. Frequency Feedforward to the RPCL

In order to keep the desired original steady-state characteristics and not to deteriorate the frequency performance, a synchronization stability enhancement method is proposed, as shown in Fig. 6. The additional path, by feedforwarding the frequency difference between the VSG and grid, is introduced into the RPCL. Since ω is equal to ω_g at the steady state, the additional path does not influence the steady-state characteristics.

From Fig. 6, it can be seen that the reactive power control law is different from (3), and it is given as

$$V_{mref} = V_0 + K_q\left(Q_{ref} - Q\right) + K_q K\left(\Delta\omega + \omega_0 - \omega_g\right). \quad (12)$$

Substituting (5) into (12), combining with $V_{pcc} = V_{mref}$ and $R_g = 0$, the relationship between V_{pcc} and δ, $\Delta\omega$, i.e., $V_{pcc}(\delta, \Delta\omega)$, can be solved, as given in (13) shown at the bottom of this page. Since the added term in (12) is zero at steady state, the additional path will not affect the steady-state characteristics.

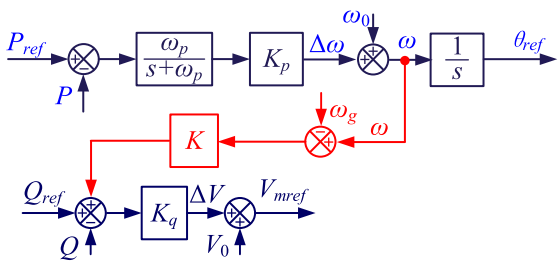

Fig. 6. Diagram of the enhanced method for synchronization stability by frequency feedforward to RPCL.

A. Qualitative Analysis Based on the Linearized System

The dynamic representation of the system is a second-order state equation, derived as

$$\begin{bmatrix}\dot{x}_1\\ \dot{x}_2\end{bmatrix} = \begin{bmatrix} x_2 + \omega_0 - \omega_g \\ -\omega_p x_2 - \frac{3\omega_p K_p V_g}{2X_g} F(x_1, x_2) + \omega_p K_p P_{ref}\end{bmatrix} \quad (14)$$

where $F(x_1, x_2)$ is

$$F(\delta, \Delta\omega) = V_{pcc}(\delta, \Delta\omega)\sin\delta. \quad (15)$$

By setting the differential of $\boldsymbol{x}$ in (14) to zero, the two equilibrium points $\boldsymbol{x_e} = [\delta_e, \Delta\omega_e]^T$ and $\boldsymbol{x_{ce}} = [\delta_{ce}, \Delta\omega_{ce}]^T$ are obtained, which are the SEP b and UEP b_1, respectively. To linearize the nonlinear system at $\boldsymbol{x_e}$, the Jacobian $\boldsymbol{J}(\boldsymbol{x_e})$ is evaluated as

$$\mathbf{J}(\mathbf{x_e}) = \begin{bmatrix} 0 & 1 \\ J_{21} & -\omega_p + J_{22}\end{bmatrix} \quad (16)$$

where J_{21} and J_{22} are expressed as

$$J_{21} = -\frac{3\omega_p K_p V_g}{2X_g} F'(\delta_e) \quad (17)$$

$$J_{22} = -\frac{3\omega_p K_p V_g}{2X_g} F'(\Delta\omega_e). \quad (18)$$

From (13) and (15), the values of the functions $F'(\delta)$ and $F'(\Delta\omega)$ around $\boldsymbol{x_e}$, i.e., $F'(\delta_e)$ and $F'(\Delta\omega_e)$, can be derived as

$$F'(\delta_e) = V_{pcce}\cos\delta_e - \frac{3K_q V_g V_{pcc_e}\sin\delta_e\sin\delta_e}{2X_g + 3K_q\left(2V_{pcce} - V_g\cos\delta_e\right)} \quad (19)$$

$$F'(\Delta\omega_e) = \frac{2X_g K_q K\sin\delta_e}{2X_g + 3K_q\left(2V_{pcce} - V_g\cos\delta_e\right)}. \quad (20)$$

Solving the characteristic equation, i.e., $\det[\lambda\boldsymbol{I} - \boldsymbol{J}(\boldsymbol{x_e})] = 0$, the eigenvalues are calculated as

$$\lambda_{1,2} = \frac{-\omega_p + J_{22} \pm \sqrt{\left(-\omega_p + J_{22}\right)^2 + 4J_{21}}}{2}. \quad (21)$$

$$V_{pcc}(\delta, \Delta\omega) = \frac{1.5K_q V_g\cos\delta - X_g + \sqrt{\left(X_g - 1.5K_q V_g\cos\delta\right)^2 + 6K_q X_g\left(V_0 + K_q Q_{ref} + K_q K\left(\Delta\omega + \omega_0 - \omega_g\right)\right)}}{3K_q} \quad (13)$$

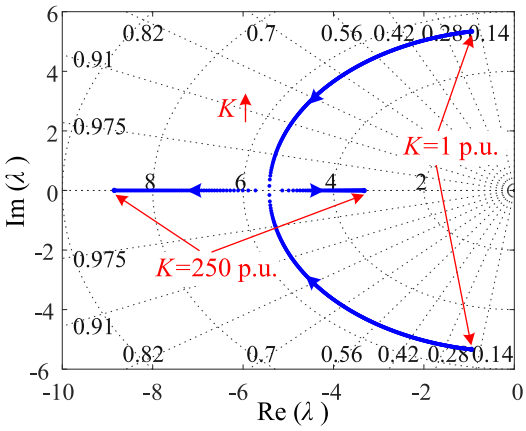

Fig. 7. Loci of eigenvalues for the second-order system in (16) with K increasing from 1 to 250 p.u. ($\omega_p = 0.6\pi$ rad/s and $V_g = 0.6$ p.u.).

Therefore, the damping ratio of the second-order system can be derived as

$$\begin{aligned}\zeta &= \frac{\omega_p - J_{22}}{2\sqrt{-J_{21}}} \\ &= \sqrt{\frac{X_g\omega_p}{6V_g K_p F'(\delta_e)}} + F'(\Delta\omega)\sqrt{\frac{3\omega_p K_p V_g}{8X_g F'(\delta_e)}}.\end{aligned} \tag{22}$$

Here, the sign of $F'(\delta_e)$ and $F'(\Delta\omega_e)$ need to be first illustrated. Suppose when $\delta = \delta_m$, $P(\delta_m) = P_{max}$ in Fig. 2(a), and thus, $\frac{\mathrm{dP}}{\mathrm{d}\delta}|_{\delta_m} = 0$. According to (4) and (15), $F'(\delta_m) = 0$ is derived. As P is monotonically increasing with δ when $\delta < \delta_m$. Therefore, when $\delta < \delta_m$, $\frac{\mathrm{dP}}{\mathrm{d}\delta} > 0$, then $F'(\delta_e) > 0$ is obtained. Meanwhile, due to $V_{pcc} \approx V_g$ in steady state, then $F'(\Delta\omega) > 0$ always holds, and it becomes larger with the increase of K.

According to (22), it can be clearly seen that ζ is related to the system parameters and controller parameters. For a given condition, the system parameters are constant. Controller parameters K_p and ω_p are related to the inertia and frequency governor, which also should be fixed. Without the additional path, the original damping ratio can be derived similarly, which is the first term in (22). Obviously, the damping ratio can be increased with the additional path, and a larger K leads to a larger damping ratio. Moreover, numerical calculations of the eigenvalues are performed with various K. The corresponding loci are plotted in Fig. 7. As shown in Fig. 7, the damping ratio increases while K becomes larger, and even an overdamped dynamics can be achieved with a sufficiently large K.

To analyze the frequency response in the s-domain, the active power P should be linearized firstly around b, given as

$$\begin{aligned}\hat{P} &= \frac{3V_g}{2X_g}\left(F'(\delta_e)\hat{\delta} + F'(\Delta\omega_e)\Delta\hat{\omega}\right) \\ \overset{\text{define}}{\Rightarrow} G_1 &= \frac{3V_g}{2X_g}F'(\delta_e) \quad G_2 = \frac{3V_g}{2X_g}F'(\Delta\omega_e)\end{aligned} \tag{23}$$

where cap (^) represents the small variations, G_1 and G_2 are the approximate gains between P and δ, P and $\Delta\omega$ evaluated at b, respectively.

Combining (23) and Fig. 1, the control block diagram is derived as in Fig. 8, where the effects of RPCL and the frequency feedforward path are equivalently substituted into APCL. From there, the dynamics of δ and $\Delta\omega$, can be described in the

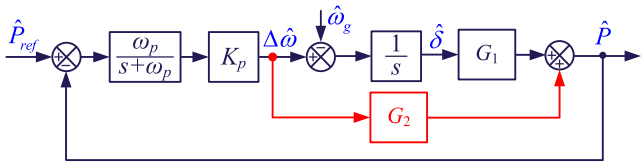

Fig. 8. Control block diagram of the VSG system with the frequency feedforward path.

s-domain as

$$\frac{\hat{\delta}}{\hat{P}_{ref}} = \frac{K_p\omega_p}{s^2 + (\omega_p + \omega_p K_p G_2)\, s + K_p\omega_p G_1} \tag{24}$$

$$\frac{\Delta\hat{\omega}}{\hat{P}_{ref}} = \frac{K_p\omega_p s}{s^2 + (\omega_p + \omega_p K_p G_2)\, s + K_p\omega_p G_1}. \tag{25}$$

The damping ratio can also be deduced from (24) and (25), which is the same as that in (22).

Assuming that the power reference has a step change, the Laplace form is 1/s. Thus, according to (25), the response of the frequency variation in the s-domain can be deduced as

$$\Delta\hat{\omega} = \frac{K_p\omega_p}{s^2 + (\omega_p + \omega_p K_p G_2)\, s + K_p\omega_p G_1}. \tag{26}$$

Rewrite (26) in the standard form of the second-order system, expressed as

$$\Delta\hat{\omega} = \frac{\omega_n^2/G_1}{s^2 + 2\zeta\omega_n s + \omega_n^2} \tag{27}$$

where $\omega_n^2 = K_p\omega_p G_1$, $2\zeta\omega_n = \omega_p + \omega_p K_p G_2$.

Thus, the response of frequency variation in the time-domain can be derived as

$$\Delta\hat{\omega} = \frac{1}{G_1}\frac{\omega_n^2}{\sqrt{1-\zeta^2}} e^{-\zeta\omega_n t}\sin\left(\sqrt{1-\zeta^2}\omega_n t\right). \tag{28}$$

The RoCoF is the change rate of frequency, which can be deduced as

$$\begin{aligned}RoCoF &= \frac{d\omega}{dt} = \frac{d\Delta\omega}{dt} \\ &= \frac{1}{G_1}\frac{\omega_n^2}{\sqrt{1-\zeta^2}} e^{-\zeta\omega_n t}\sin\left(\beta - \sqrt{1-\zeta^2}\omega_n t\right)\end{aligned} \tag{29}$$

where $\sin\beta = \sqrt{1-\zeta^2}$.

The maximum RoCoF is achieved when $t = 0$, which is calculated as

$$RoCoF|_{max} = \frac{1}{G_1}\frac{\omega_n^2}{\sqrt{1-\zeta^2}}\sin(\beta) = K_p\omega_p = \frac{1}{J}. \tag{30}$$

It can be found that the inertia J determines the maximum RoCoF, which has no relationship with K, indicating the additional path does not influence the maximum RoCoF. Furthermore, the inertia J should be large enough to maintain the maximum RoCoF in the acceptable range according to the grid code [8].

When the derivative of frequency is equal to zero, the maximum frequency variation can be obtained, given as

$$\Delta\hat{\omega}|_{max} = \omega_n e^{-\frac{\zeta}{\sqrt{1-\zeta^2}}\arcsin\left(\sqrt{1-\zeta^2}\right)} \approx \sqrt{\frac{G_1}{J}} e^{-\zeta}. \tag{31}$$

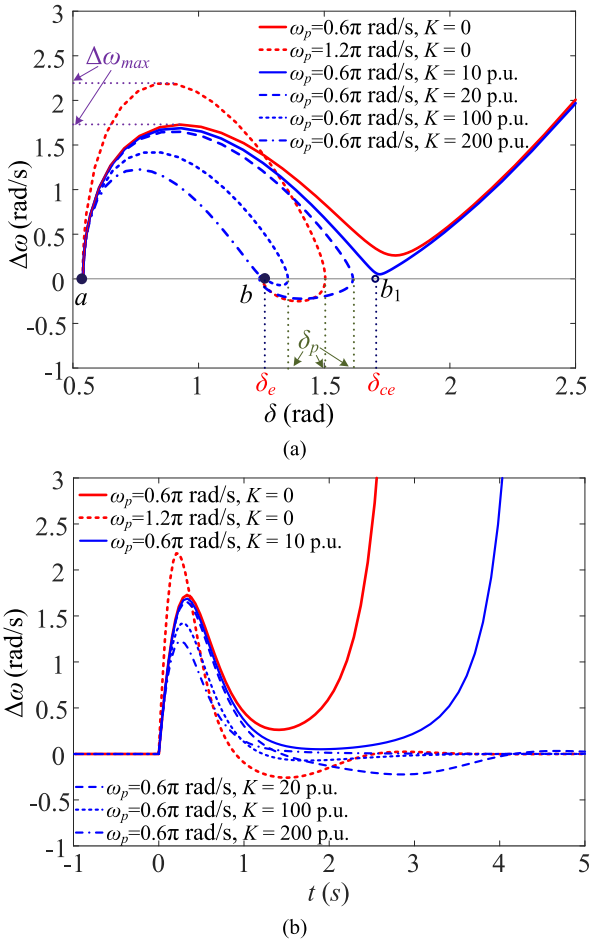

Fig. 9. VSG responses with different K in the frequency feedforward path when $V_g = 1 \rightarrow 0.6$ p.u. (a) Trajectories of the nonlinear system in the phase plane. (b) Frequency response in the time domain.

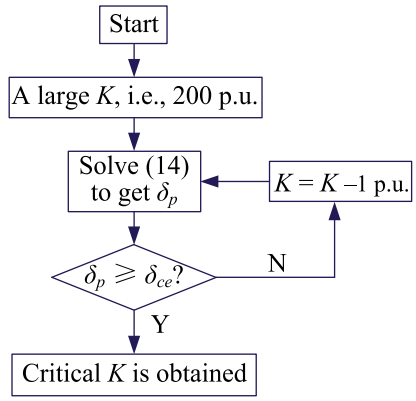

Fig. 10. Iterative calculation procedure of the critical value of K for a specific ω_p.

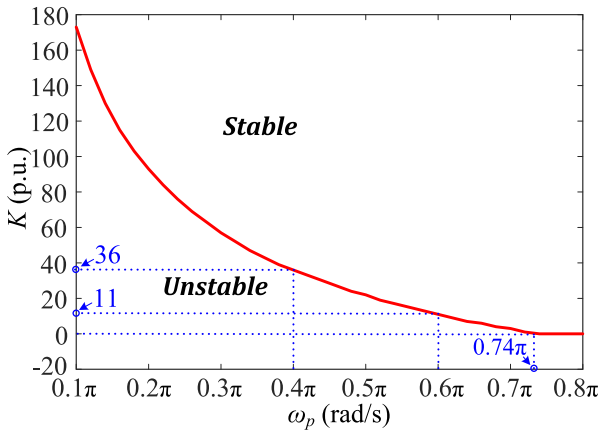

Fig. 11. Minimum required K according to different inertia requirements (different ω_p) when $V_g = 1 \rightarrow 0.6$ p.u.

As can be seen from (31), the maximum frequency deviation is an inverse ratio of J and ζ. Increasing J is unexpected from the perspective of synchronization stability [21]. Thus, increasing ζ can effectively decrease the frequency deviation during the transient period, which perfectly avoids the conflict between frequency stability and synchronization stability.

Therefore, the additional frequency feedforward path with a larger K, leading to a larger damping ratio, which enhances synchronization stability and simultaneously benefits frequency stability during grid fault.

B. Quantitative Analysis Based on the Nonlinear System

The influence of the proposed method on exact transient behaviors is examined in Fig. 9 based on the nonlinear system in (14). It can be observed that without the additional path, an LOS occurs when the grid voltage drops from 1 to 0.6 p.u. with $\omega_p = 0.6\pi$ rad/s, due to the low-damping dynamics. Increasing ω_p to 1.2π rad/s (the virtual inertia J is decreased) can remove the instability due to an increased ζ.

However, the frequency response becomes worse, i.e., a larger $\Delta\omega_{\max}$ and higher RoCoF are observed, resulting from smaller inertia. The frequency feedforward method can also remove the instability with a large K. It can be seen that the overshoot of δ can be reduced with a larger K due to the increased ζ. Even an overdamped response can be achieved by a sufficiently large K, i.e., $K = 200$ p.u. Moreover, $\Delta\omega_{max}$ decreases with the increase of K, which is also helpful to frequency stability. Therefore, a larger K is expected to increase the damping ratio, thus improving the synchronization stability and frequency stability. Otherwise, instability can occur if K is not large enough, i.e., $K = 10$ p.u. The system suffers from poorly damped dynamics, which causes δ to exceed δ_{ce}.

A larger K is expected from the abovementioned analysis, but an extensive K is also not practical. Thus, the minimum required K according to different inertia requirements should be found. This is also handy design information for engineers to identify how far or close the system is from the LOS region. As only if δ exceeds δ_{ce}, LOS can occur. Thus, as long as δ_p does not exceed δ_{ce}, the synchronization stability can be guaranteed. According to this, the critical value of K for each specified ω_p can be calculated using the procedure in Fig. 10, which is plotted in Fig. 11. In Fig. 11, the stable and unstable operation regions are located above and below the boundary line, respectively. From them, it can be found that smaller ω_p (larger J), the minimum required K for the stable operation increases. For example, with

TABLE II
METHODS TO IMPROVE THE TRANSIENT STABILITY OF THE VSG

Methods	Affecting the steady-state performance	Enhancement of synchronization stability	Enhancement of frequency stability	Implementation complexity
Change active and reactive power references [26] [27]	Yes	Good	Poor	Low
Adaptive inertia [29][30]	No	Medium	Good	Medium
Additional damping control [31]	No	Medium	Medium	Medium
Mode-switching control [32]	No	Good	Not discussed	High
Decrease the bandwidth of LPF in RPCL [21]	No	Poor	Not discussed	Low
Frequency feedforward added on RPCL	No	Medium	Good	Low

$\omega_p = 0.6\pi$ rad/s, it is sufficient when $K > 11$ p.u., but if $\omega_p = 0.4\pi$ rad/s, then $K > 36$ p.u. must be adopted. Hence, using the frequency feedforward to the RPCL method with a larger K, higher inertia becomes viable.

Combining with the analysis in Section IV-A, a larger J can reduce RoCoF of the system. Meanwhile, a larger K increases the damping ratio, which reduces the power angle overshoot and frequency deviation during the transient period. Therefore, by adjusting J and K together, both the transient stability and frequency stability can be improved.

C. Comparison of Transient Stability Enhancement Methods

Different transient stability enhancement methods have distinct performance, a comparison of which is listed in Table II from different perspectives. Four indicators are selected to compare as follows: steady-state performance, enhancement of synchronization stability, enhancement of frequency stability, and implementation complexity.

1) Steady-state performance: changing the steady-state performance does not satisfy the IEEE standard 1547-2018. Thus, whether affecting the steady-state performance is a significant index during riding through the grid faults.
2) Enhancement of synchronization stability: all the enhancement methods can improve synchronization stability when the VSG has an equilibrium point. However, just [32] can damp the oscillation within a small bounded range even without an equilibrium point, which can be regarded as a good performance of improving synchronization stability.
3) Enhancement of frequency stability: if the method can decrease the RoCoF and maximum frequency deviation simultaneously, it can be classified as a good frequency stability performance.
4) Implementation complexity: if the method contains differential detecting elements during the transient process, it may reduce the anti-interference performance. This kind of method is classified as having a high implementation complexity.

Based on these four indexes, it can be seen that the frequency feedforward method proposed in this article is a compromise between the synchronization stability and implementation complexity.

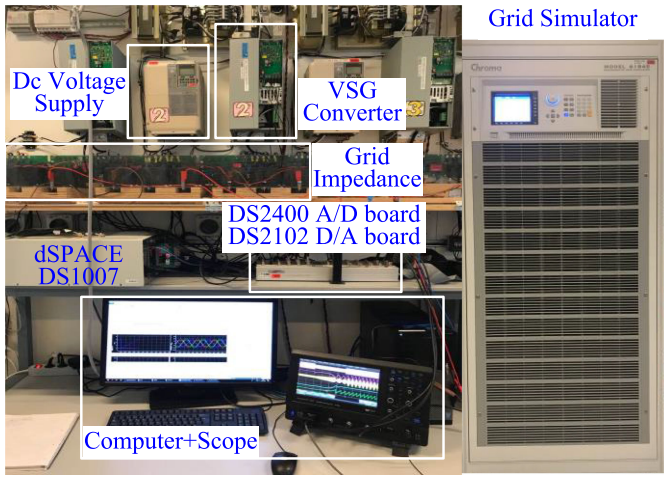

Fig. 12. Experimental setup.

It should be noted that although only a grid voltage sag has been considered in this article, the analytical method and the proposed method to enhance synchronization stability can be similarly also applied to other types of fault, such as grid impedance jumps. Since the synchronization stability of the grid-forming converters is ongoing work, more analyzing methodologies and the synchronization stability enhancement methods for the multi-inverter system will be studied in the future.

V. EXPERIMENTAL VERIFICATION

To verify the theoretical analysis and the effectiveness of the proposed frequency feedforward method, an experimental setup is established in the lab, as shown in Fig. 12. The dc voltage is provided by another rectifier. A Chroma 61850 grid simulator connected in series with a three-phase inductor is employed to emulate the weak power grid. The voltage and current are measured by the dSPACE DS2004 A/D board and then sent to the dSPACE DS1007 platform, where the control strategies are implemented. The calculated P, δ, and the signal $\Delta\omega$ are transmitted to the oscilloscope through the DS2102 D/A board

The VSG's main parameters are given in Table III, where K_p and K_q are chosen according to their droop functions demanded in grid codes like in [20] and [21]. The transient performances of

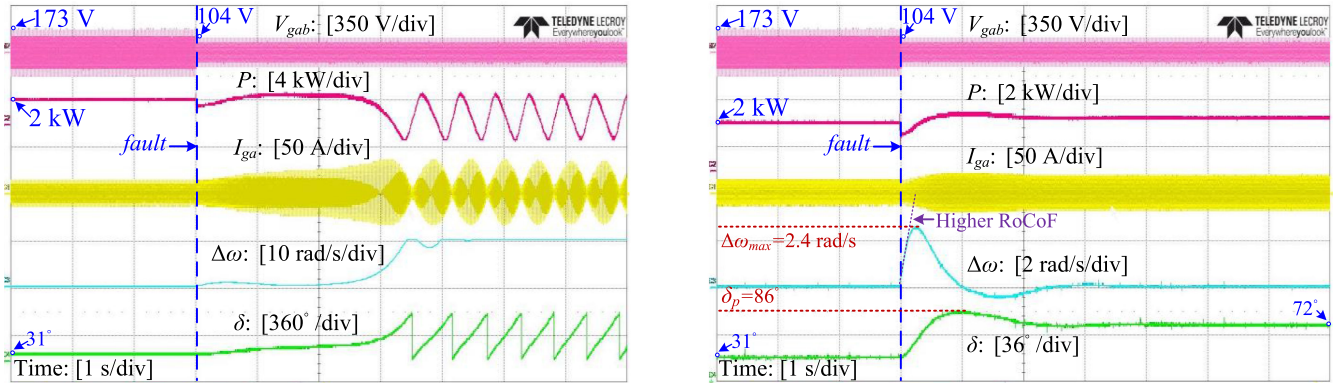

Fig. 13. Experimental results of the VSG without the frequency feedforward path ($K_2 = 0$) when V_g drops from 1 to 0.6 p.u. The Scenario A in Table IV is tested as (a) Case I: $\omega_p = 0.6\pi$ rad/s and (b) Case II: $\omega_p = 1.2\pi$ rad/s.

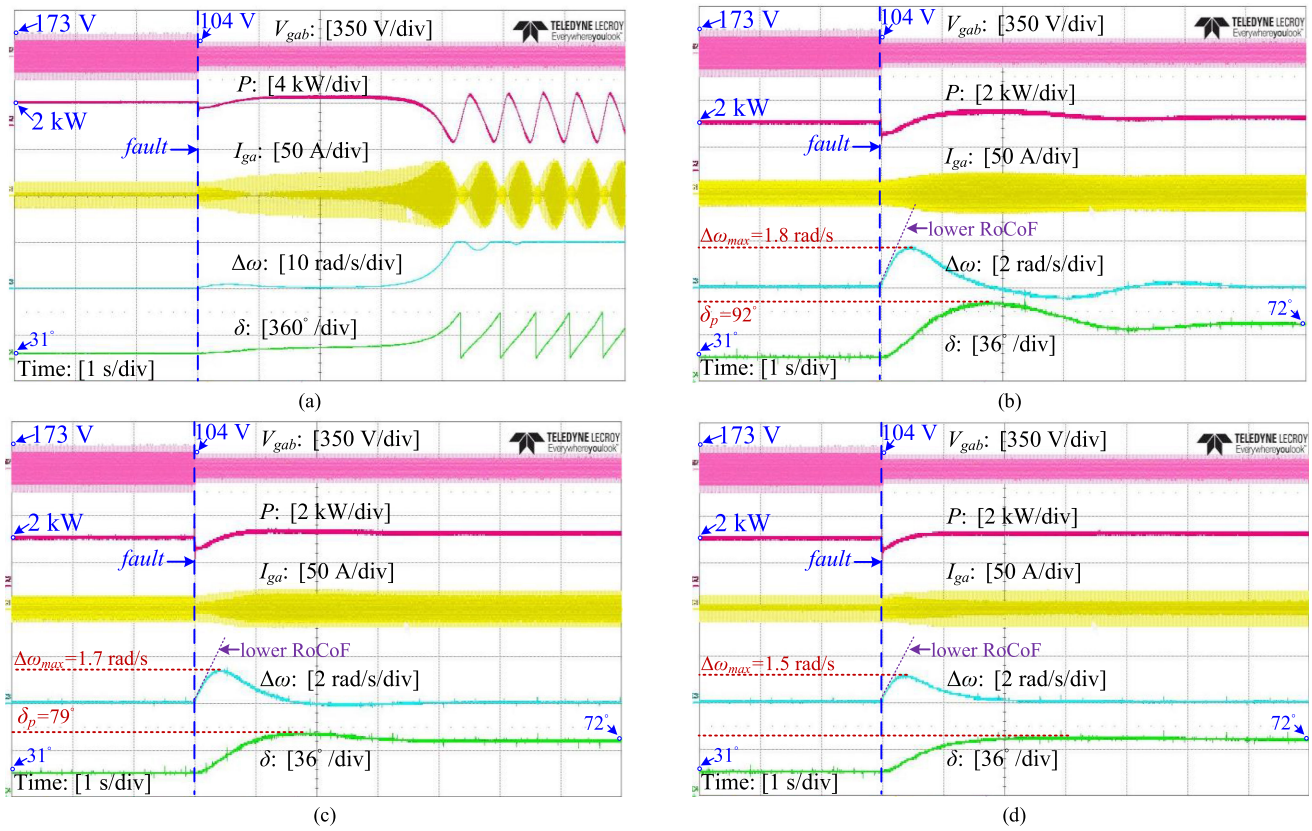

Fig. 14. Experimental results of the VSG with the addtional frequency feedforward path in the RPCL when V_g drops from 1 to 0.6 p.u. The Scenario B in Table IV is tested as (a) Case I: $K = 10$ p.u., (b) Case II: $K = 20$ p.u., (c) Case III: $K = 100$ p.u., and (d) Case IV: $K = 200$ p.u. $\omega_p = 0.6\pi$ rad/s is used for the four cases.

the VSG under the grid voltage dropping from 1 to 0.6 p.u. are evaluated. In order to perform a comparative verification, three types of scenarios with different sets of ω_p and K are examined, as shown in Table IV. The corresponding experimental results are shown in Figs. 13–15. From top to bottom in each figure, the displayed waveforms are the phase to phase voltage V_{gab}, the active power P, the line current of phase a, i.e., I_{ga}, the deviation of frequency $\Delta\omega$ and power angle δ, respectively.

In Fig. 13, the original system without the additional frequency feedforward path is tested. In Fig. 13(a), an instability occurs when V_g drops from 1 to 0.6 p.u. due to a small ω_p leading to a small damping ratio for the power angle. This instability can be removed by increasing ω_p, i.e., ω_p is increased to 1.2π rad/s, as shown in Fig. 13(b). However, a larger ω_p implies smaller virtual inertia. Thereby, a larger $\Delta\omega_{max}$ and higher RoCoF are observed in Fig. 13(b). These experimental results verify the

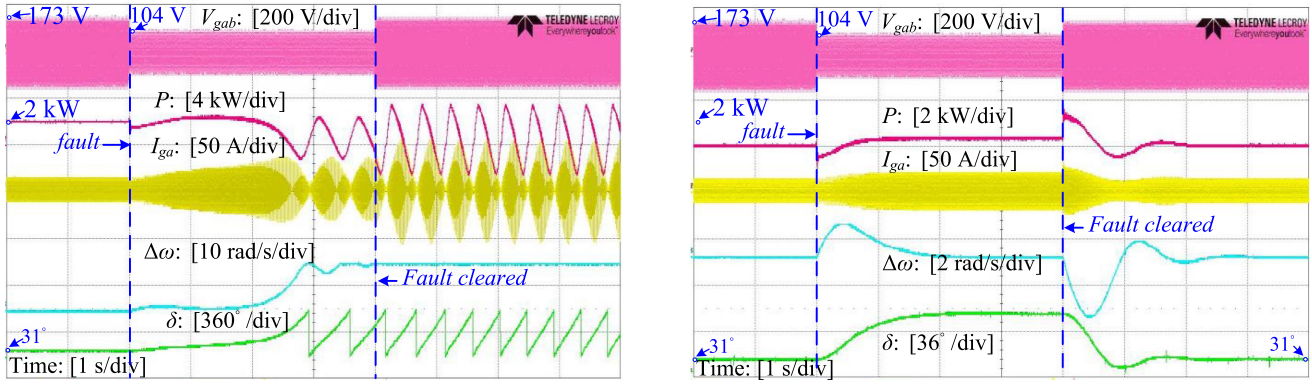

Fig. 15. Experimental results of the VSG with $\omega_p = 0.6\pi$ rad/s when V_g drops from 1 to 0.6 p.u. and recovers after 4 s. The Scenario C in Table IV is tested as (a) Case I: $K = 0$ p.u., and (b) Case II: $K = 20$ p.u.

TABLE III
MAIN PARAMETERS OF THE VSG SYSTEM USED IN THE EXPERIMENTS

Parameters	Description	Value	p.u.
P_{ref}	Rated active power	2 kW	1.0
Q_{ref}	Rated reactive power	0	0
V_0	Rated voltage	100 V	1.0
V_g	Normal grid voltage	100 V	1.0
ω_0	Grid angular frequency	314 rad/s	
L_g	Grid inductance	12 mH	0.5
K_p	P-f droop gain	$0.04\omega_0/P_{\max}$	0.04
K_q	Q-V droop gain	$0.1V_0/Q_{\max}$	0.1
K	Additional coefficient	$1\ Q_{\max}/V_0$	1

TABLE IV
DIFFERENT SETS OF CONTROL PARAMETERS USED IN THE EXPERIMENTS

Parameter	Scenario A		Scenario B				Scenario C	
	I	II	I	II	III	IV	I	II
ω_p (π rad/s)	0.6	1.2	0.6	0.6	0.6	0.6	0.6	0.6
K (p.u.)	0	0	10	20	100	200	0	20

theoretical analysis on the frequency response, as the red lines are shown in Fig. 9.

Then, the proposed frequency feedforward path was added to the RPCL with different parameter settings. The experimental results are shown in Fig. 14. It can be seen that the grid voltage sag can also trigger an LOS due to the poor damping dynamics with a small K, i.e., $K = 10$ p.u. Increasing K, the system can be stabilized, and the overshoot of δ declines due to the damping ratio increases. The power angle overshoot can be completely damped with large enough K, i.e., $K = 200$ p.u. These results agree with the theoretical analysis in Section IV.

Moreover, it can be seen that the additional frequency feedforward path with a large K not only reduces the overshoot of δ during the fault but also reduces $\Delta\omega_{max}$. These experimental results validate the analyzed theoretical results, confirming the effectiveness of the proposed frequency feedforward method. Therefore, this method can enhance the synchronization stability of the VSG without degrading the frequency stability.

According to IEEE Standards 1547-2018 [28], the VSG should continue to supply power at least for 10 s when the grid voltage drops to 0.6 p.u. Thus, the fault is not cleared in Figs. 13 and 14, since riding-through the low voltage is more severe than the period of grid voltage coming back to normal. Thus, as long as the VSG is controlled stable during the fault, the synchronization stability can be guaranteed when the fault is cleared after 10 s. To prove this, Fig. 15 gives the experimental results of clearing the fault after 4 s (for convenience of displaying). From there, it can be seen that if an LOS occurs during the fault, the system cannot return to stable operation after the fault is cleared. However, when the additional frequency feedforward path is added to improve the stability during the fault, i.e., $K = 20$ in Fig. 15(b), the system can remain stable after the fault is cleared.

VI. CONCLUSION

First, combined linearized and nonlinear model are employed to analyze synchronization stability. The linearized model is used for qualitative analysis, while quantitative analysis is according to the nonlinear model. Second, based on the combined model, the mechanism of employing LPF in the RPCL to enhance synchronization stability is revealed. It indicates that an LPF with a sufficiently low cutoff frequency introduces a dominant closed-loop pole for the original second-order dynamic system and can damp the power angle overshoot oscillation, leading to a better transient power angle response. Third, an improved synchronization method is proposed by feedforwarding the frequency to RPCL, which can avoid the slow dynamic LPF in RPCL. Parameter design guidelines are given to enhance the synchronization stability with different inertia requirements, which indicates a larger coefficient of the feedforward path is expected with larger inertia. Fourth, the frequency response is also deduced based on the combined model, demonstrating that the improved synchronization methods can further improve the frequency stability during grid faults. Finally, experimental results have verified the effectiveness of the theoretical analysis and the proposed method.

REFERENCES

[1] F. Blaabjerg, R. Teodorescu, M. Liserre, and A. V. Timbus, "Overview of control and grid synchronization for distributed power generation systems," *IEEE Trans. Ind. Electron.*, vol. 53, no. 5, pp. 1398−1409, Oct. 2006.

[2] F. Blaabjerg, Y. Yang, D. Yang, and X. Wang, "Distributed power-generation systems and protection," *Proc. IEEE*, vol. 105, no. 7, pp. 1311–1331, Jul. 2017.

[3] J. Liu, Y. Miura, H. Bevrani, and T. Ise, "A unified modeling method of virtual synchronous generator for multi-operation-mode analyses," *IEEE J. Emerg. Sel. Topics Power Electron.*, early access, 2020.

[4] J. Quintero, V. Vittal, G. T. Heydt, and H. Zhang, "The impact of increased penetration of converter control-based generators on power system modes of oscillation," *IEEE Trans. Power Syst.*, vol. 29, no. 5, pp. 2248–2256, Sep. 2014.

[5] M. Dreidy, H. Mokhlis, and S. Mekhilef, "Inertia response and frequency control techniques for renewable energy sources: A review," *Renew. Sust. Energ. Rev.*, vol. 69, pp. 144–155, Mar. 2017.

[6] J. Fang, H. Li, Y. Tang, and F. Blaabjerg, "On the inertia of future more-electronics power systems," *IEEE J. Emerg. Sel. Topics Power Electron.*, vol. 7, no. 4, pp. 2130–2146, Dec. 2019.

[7] M. Chen, D. Zhou, and F. Blaabjerg, "Modelling, implementation, and assessment of virtual synchronous generator in power systems," *J. Mod. Power Syst. Clean Energy*, vol. 8, no. 3, pp. 399–411, May 2020.

[8] S. D. Arco, J. A. Suul, and O. B. Fosso, "A virtual synchronous machine implementation for distributed control of power converters in smartgrids," *Elect. Power Syst. Res.*, vol. 122, pp. 180−197, May 2015.

[9] D. Chen, Y. Xu, and A. Q. Huang, "Integration of dc microgrids as virtual synchronous machines into the ac grid," *IEEE Trans. Ind. Electron.*,vol. 64, no. 9, pp. 7455–7466, Sep. 2017.

[10] S. A. Khajehoddin, M. Karimi-Ghartemani, and M. Ebrahimi, "Grid supporting inverters with improved dynamics," *IEEE Trans. Ind. Electron.*, vol. 66, no. 5, pp. 3655–3667, May 2019.

[11] Y. Chen *et al.*, "Dynamic properties of the virtual synchronous machine (VISMA)," *Renew. Energy Power Qual. J.*, vol. 1, no. 9, pp. 755–759, May 2011.

[12] Q. C. Zhong and G. Weiss, "Synchronverters: Inverters that mimic synchronous generators," *IEEE Trans. Ind. Electron.*, vol. 58, no. 4, pp. 1259−1267, Apr. 2011.

[13] Y. Deng, Y. Tao, G. Chen, G. Li, and X. He, "Enhanced power flow control for grid-connected droop-controlled inverters with improved stability," *IEEE Trans. Ind. Electron.*, vol. 64, no. 7, pp. 5919−5929, Jul. 2017.

[14] X. Meng, J. Liu, and Z. Liu, "A generalized droop control for grid-supporting inverter based on comparison between traditional droop control and virtual synchronous generator control," *IEEE Trans. Power Electron.*, vol. 34, no. 6, pp. 5416−5438, Jul. 2019.

[15] J. Liu, Y. Miura, and T. Ise, "Comparison of dynamic characteristics between virtual synchronous generator and droop control in inverter-based distributed generators," *IEEE Trans. Power Electron.*, vol. 31, no. 5, pp. 3600–3611, May 2016.

[16] H. Yu, M. A. Awal, H. Tu, I. Husain, and S. Lukic, "Comparative transient stability assessment of droop and dispatchable virtual oscillator controlled grid-connected inverters," *IEEE Trans. Power Electron.*, vol. 36, no. 2, pp. 2119–2130, Feb. 2021.

[17] D. Li, Q. Zhu, S. Lin, and X. Y. Bian, "A self-adaptive inertia and damping combination control of VSG to support frequency stability," *IEEE Trans. Energy Convers.*, vol. 32, no. 1, pp. 397–398, Mar. 2017.

[18] M. A. Torres L., L. A. C. Lopes, L. A. Moran T., and J. R. Espinoza C., "Self-tuning virtual synchronous machine: A control strategy for energy storage systems to support dynamic frequency control," *IEEE Trans. Energy Convers.*, vol. 29, no. 4, pp. 833–840, Dec. 2014.

[19] S. Dong and Y. C. Chen, "Adjusting synchronverter dynamic response speed via damping correction loop," *IEEE Trans. Energy Convers.*, vol. 32, no. 2, pp. 608–619, Jun. 2017.

[20] H. Wu *et al.*, "Small-signal modeling and parameters design for virtual synchronous generators," *IEEE Trans. Ind. Electron.*, vol. 64, no. 7, pp. 4292–4303, Jul. 2016.

[21] D. Pan, X. Wang, F. Liu, and R. Shi, "Transient stability of voltage-source converters with grid-forming control: A design-oriented study," *IEEE J. Emerg. Sel. Topics Power Electron.*, vol. 8, no. 2, pp. 1019–1033, Jun. 2020.

[22] D. G. A. Krishna, K. Anbalagan, K. K. Prabhakaran, and S. Kumar, "An efficient pseudo derivative feedback based voltage controller for DVR under distorted grid conditions," *IEEE J. Emerg. Sel. Topics Ind. Electron.*, vol. 2, no. 1, pp. 71–81, Jan. 2021.

[23] C. Tu *et al.*, "Dynamic voltage restorer with an improved strategy to voltage sag compensation and energy self-recovery," *CPSS Trans. Power Electron. Appl.*, vol. 4, no. 3, pp. 219–229, Sep. 2019.

[24] X. Wang, M. G. Taul, H. Wu, Y. Liao, F. Blaabjerg, and L. Harnefors, "Grid-synchronization stability of converter-based resources—An overview," *IEEE Open J. Ind. Appl.*, vol. 1, pp. 115–134, 2020.

[25] H. Wu and X. Wang, "Design-oriented transient stability analysis of grid connected converters with power synchronization control," *IEEE Trans. Ind. Electron.*, vol. 66, no. 8, pp. 6473–6482, Aug. 2019.

[26] Z. Shuai, C. Shen, X. Liu, Z. Li, and Z. J. Shen, "Transient angle stability of virtual synchronous generators using Lyapunov's direct method," *IEEE Trans. Smart Grid*, vol. 10, no. 4, pp. 4648–4661, Jul. 2019.

[27] D. Pan, X. Wang, F. Liu, and R. Shi, "Transient stability impact of reactive power control on grid-connected converters," in *Proc. IEEE Energy Convers. Congr. Expo.*, 2019, pp. 4311–4316.

[28] *IEEE Standard for Interconnection and Interoperability of Distributed Energy Resources With Associated Electric Power Systems Interfaces*, IEEE Std 1547-2018, Apr. 6, 2018.

[29] J. Alipoor, Y. Miura, and T. Ise, "Power system stabilization using virtual synchronous generator with alternating moment of inertia," *IEEE J. Emerg. Sel. Topics Power Electron.*, vol. 3, no. 2, pp. 451–458, Jun. 2015.

[30] X. Hou, H. Han, C. Zhong, W. Yuan, M. Yi, and Y. Chen, "Improvement of transient stability in inverter-based AC microgrid via adaptive virtual inertia," in *Proc. IEEE Energy Convers. Congr. Expo.*, Sep. 2016, pp. 1–6.

[31] H. Cheng, Z. Shuai, C. Shen, X. Liu, Z. Li, and Z. J. Shen, "Transient angle stability of paralleled synchronous and virtual synchronous generators in islanded microgrids," *IEEE Trans. Power Electron.*, vol. 35, no. 8, pp. 8751–8765, Aug. 2020.

[32] H. Wu and X. Wang, "A mode-adaptive power-angle control method for transient stability enhancement of virtual synchronous generators," *IEEE J. Emerg. Sel. Topics Power Electron.*, vol. 8, no. 2, pp. 1034–1049, Jun. 2020.

[33] X. Xiong and X. Ruan, "Non-smooth bifurcation analysis of multi-structure multi-operating-mode power electronics systems for applications with renewable energy sources," *IEEE Trans. Circuits Syst. II Exp. Briefs*, vol. 66, no. 3, pp. 487–491, Mar. 2019.

[34] P. Pan *et al.*, "An impedance-based stability assessment methodology for DC distribution power system with multivoltage levels," *IEEE Trans. Power Electron.*, vol. 35, no. 4, pp. 4033–4047, Apr. 2020.

[35] H. Yuan, X. Yuan, and J. Hu, "Modeling of grid-connected VSCs for power system small-signal stability analysis in DC-link voltage control timescale," *IEEE Trans. Power Syst.*, vol. 32, no. 5, pp. 3981−3991, Sep. 2017.

[36] L. Harnefors, X. Wang, A. Yepes, and F. Blaabjerg, "Passivity-based stability assessment of grid-connected VSCs—An overview," *IEEE J. Emer. Select. Topics Power Electron.*, vol. 4, no. 1, pp. 116–125, Mar. 2016.

Xiaoling Xiong (Member, IEEE) received the B.S., M.S., and Ph.D degrees in electrical engineering from Nanjing University of Aeronautics and Astronautics, Nanjing, China, in 2007, 2010, and 2015, respectively.

She was a Research Assistant with the Department of Electronic and Information Engineering, Hong Kong Polytechnic University, Hong Kong, from February 2011 to July 2012. Since 2015, she has been with North China Electric Power University, Beijing, China, where she was a Lecturer. From December 2018 to November 2020, she was with Aalborg University, Aalborg, Denmark, where she was a Visiting Postdoctoral with the Department of Energy Technology. Her current research interests include HVdc system, modeling, analysis and design power electronic systems, and study the nonlinear behaviors in power electronic circuits.

Chao Wu (Member, IEEE) was born in Hubei Province, China. He received the B.Eng. degree from Hefei University of Technology, Hefei, China in 2014, and the Ph.D. degree from Zhejiang University, Hangzhou, China, in 2019, both in electrical engineering.

He is currently a Postdoctoral Researcher with the Department of Energy Technology, Aalborg University, Aalborg, Denmark. His current research interests include cooperative control of multiconverter systems, particularly the control and operation of doubly fed induction generators for dc connection, and the transient stability of power converters.

Frede Blaabjerg (Fellow, IEEE) received the Ph.D. degree in electrical engineering from Aalborg University, Aalborg, Denmark, in 1995. He is currently working toward the honoris causa with University Politehnica Timisoara (UPT), Timisoara, Romania, and Tallinn Technical University (TTU), Tallinn, Estonia.

He was with ABB-Scandia, Randers, Denmark, from 1987 to 1988. He became an Assistant Professor in 1992, an Associate Professor in 1996, and a Full Professor of power electronics and drives in 1998. In 2017, he became a Villum Investigator. He has authored or coauthored more than 600 journal papers in the fields of power electronics and its applications. He is the co-author of four monographs and editor of ten books in power electronics and its applications. His current research interests include power electronics and its applications such as in wind turbines, PV systems, reliability, harmonics and adjustable speed drives.

Prof. Blaabjerg was the recipient of 32 IEEE Prize Paper Awards, the IEEE PELS Distinguished Service Award in 2009, the EPE-PEMC Council Award in 2010, the IEEE William E. Newell Power Electronics Award 2014, the Villum Kann Rasmussen Research Award 2014, the Global Energy Prize in 2019, and the IEEE Edison Medal in 2020. He was the Editor-in-Chief of the IEEE TRANSACTIONS ON POWER ELECTRONICS from 2006 to 2012. He has been a Distinguished Lecturer for the IEEE Power Electronics Society from 2005 to 2007 and for the IEEE Industry Applications Society from 2010 to 2011 as well as from 2017 to 2018. In 2019–2020, he was the President of IEEE Power Electronics Society. He is also the Vice-President of the Danish Academy of Technical Sciences. He is nominated in 2014–2019 by Thomson Reuters to be between the 250 most-cited researchers in engineering in the world.